Processing-Structure-Property Relationships of bisphenol-A-Polycarbonate Samples Prepared by Fused Filament Fabrication[1]

Lichen Fang [a], Yishu Yan [a], Ojaswi Agarwal [a], Jonathan E. Seppala [b], Kevin J. Hemker [a], Sung Hoon Kang [a,*]

[a] Department of Mechanical Engineering and Hopkins Extreme Materials Institute, Johns Hopkins University, Baltimore, MD 21218, USA

[b] Materials Science and Engineering Division, National Institute of Standards and Technology, Gaithersburg, MD 20899, USA

* Corresponding author

Email address: shkang@jhu.edu

Abstract

Fused filament fabrication (FFF) is one of the most popular additive manufacturing processes. However, structural applications of FFF are still limited by unwanted variations in mechanical strength and structural dimensions of printed parts. To obtain a fundamental understanding of these issues, we focused on the interlayer bonding region of bisphenol-A-polycarbonate samples. The samples were prepared by a low-cost open-source FFF 3D printer, and full three-dimensional (3D) geometrical characterizations were performed on them using X-ray micro computed tomography (micro-CT). The results showed significant geometry variation depending on different printing conditions, including print speed, layer height, and nozzle temperature. Based on the results, we demonstrated the effects of reducing layer height and increasing nozzle temperature as well as compensating material extrusion rate to improve geometric precision with minimum 0.8 % deviation. Moreover, uniaxial tensile and Mode III tear tests results showed that there are linear relations between bonding zone geometry and bonding strength. In addition, from the 3D geometry of the resulting printed part, we could estimate the Young's modulus in the extrudate stacking direction using finite element method, which showed good agreement with the measured value. We envision that our findings can contribute to providing guidelines for the selection of printing parameters to improve or customize printing quality. Our experimental data may also serve as benchmark data for future multi-physics simulation models.

Keywords: Fused filament fabrication; X-ray computed tomography; polycarbonate; bonding zone

[1] Official contribution of the National Institute of Standards and Technology; not subject to copyright in the United States.

1. Introduction

Additive manufacturing (AM) represents a revolution in fabrication methodology. The technology provides more freedom for manufacturing complex 3D structures and allows users to easily transfer digital designs to physical items without the need of machining skills [1]. Among the various AM methods, fused filament fabrication (FFF) [2] [2] is one of the most popular processes. The low cost and straightforward operation significantly lower the bar for both professionals and nonprofessionals to manufacture prototypes, compared with using traditional manufacturing methods that generally require extensive training and expensive equipment [3]. However, the quality of FFF produced products are generally inferior to those of traditional manufacturing methods and heavily influenced by multiple processing parameters [4], which further limits more structural applications of this technology [5].

In the past few decades a large number of studies have investigated the effects of processing parameters on mechanical properties of parts fabricated by FFF. The most common variables include geometrical parameters (layer height, road width, gap between roads), thermal profiles (nozzle temperature, chamber temperature, print bed temperature), and deposition rate (print speed, material feed rate) [6 - 10]. Besides these parameters that could influence a single road property, the tool path or strategy of how to stack up extrudates also contributes to the overall mechanical performance of the part. Thus, relevant parameters, including raster angle, infill density and infill pattern, have been studied as well [11, 12]. In previous works, the most common experimental method for characterization of the printed part is uniaxial tensile test. From uniaxial tensile test and fractographic analysis, the failure modes of FFF products were studied [13]. Furthermore, by rotating the build orientation with respect to the loading direction, it is possible to measure the anisotropy of FFF specimens [14]. In addition, to focus on the bonding quality between layers, peeling tests [15] and Graves tear tests [16, 17] have been reported. The point to be noted here is that most studies experimentally investigated the mechanical properties of bulk cubic structures or multi-layer dogbone tensile specimens, rather than focusing on welding zones between adjacent layers, which are crucial for gaining fundamental understanding of the relation between process and property.

Besides mechanical properties, another important quality issue is the dimensional stability. To characterize the dimension of FFF products, there have been various studies applying different techniques, including optical microscopy [18], flatbed scanning [19], scanning electron microscopy (SEM) [4] and profilometer [20]. However, these methods are limited to dimensional accuracy and surface roughness of exterior surfaces [21]. To gain a full 3D information of the sample geometry, micro-CT is a suitable tool. Micro-CT can generate 3D digital models of a specimen by taking multiple X-ray images from different angles and reconstructing its 3D profile from the cross-sectional images [22]. Micro-CT as a method to assess quality of 3D printed part was identified in the early 90s [23] with the first application of this concept to AM process in 1997 [24]. Subsequently, micro-CT has been utilized in powder-

[2] Material Extrusion is the ASTM/ISO defined term for Fused filament fabrication (FFF), however, FFF is used more commonly in the literature. The process described as fused deposition modeling (FDM) is a trademark of Stratasys, Inc.

based AM to study the influence of porosity [25 - 27]. More recently, micro-CT technologies have been utilized for various studies of FFF prints [28], including studying the structural voids [29, 30] and air bubbles [31], assessing the dimensional accuracy and inner defects of engineering products [32, 33], investigating anisotropic effects driven by pore percolation of samples with different raster directions [29, 34], characterizing microstructural features of multi-directional preform [35] and fiber-reinforced composites [33, 36], and understanding failure mechanism combined with in-situ tensile tests [37]. Recently, there is a study focusing on the effects of fabrication temperature, studying the relationship between mechanical strength and internal geometry [38]. However, there are still no quantitative studies systematically covering all the major processing parameters in FFF, investigating the 3D geometry of interlayer bonding region, and analyzing its correlation with mechanical performance.

In this study, we selected some of the most important processing parameters: print speed, layer height, and nozzle temperature, and investigated how these parameters affect the geometrical and mechanical quality of FFF products. We extracted the geometrical data of FFF samples fabricated with different processing parameters by using micro-CT and further analyzed the data. Then, we combined the geometrical analysis with uniaxial tensile and Mode III tear test results to study effects of processing parameters on the bonding quality and the resulting geometrical and mechanical quality. Finally, we optimized the processing parameters based on the results from the study to produce FFF samples with better geometrical precision and mechanical performance.

2. Materials and methods

2.1 Materials and equipment

In this study, 2.85 mm bisphenol-A-polycarbonate (PC) filament from Ultimaker[3] was used to fabricate all the specimens. The material properties were measured with an MTS Criterion 40 uniaxial tensile tester. The filament has a diameter of 2.85 mm ± 0.02 mm, Young's modulus of 1.87 GPa ± 0.13 GPa, and a tensile strength of 71.6 MPa ± 3.6 MPa (see the section **S1** of Supplementary Materials for details). To eliminate potential void defects caused by moisture absorbed in the filament, all filaments were dried at 100 °C for 1 h prior to printing. To print parts, an open-source LulzBot TAZ 6 printer was used, which is equipped with a 0.5 mm diameter extrusion nozzle and a 280 mm by 280 mm heated build plate. An acrylic enclosure (Printed Solid, Inc.) was attached to the printer and sealed with Kapton tape. By connecting dry compressed air to the enclosure, the environmental humidity was maintained below 10 % RH to further minimize potential void defects.

[3] Certain commercial equipment, instruments, or materials are identified in this paper in order to specify the experimental procedure adequately. Such identification is not intended to imply recommendation or endorsement by the National Institute of Standards and Technology, nor is it intended to imply that the materials or equipment identified are necessarily the best available for the purpose.

2.2 FFF processing conditions

As **Fig. 1** shows, a hollow box geometry (70 mm by 70 mm by 50 mm) that was used to prepare tensile and micro-CT specimens in this study, while hollow box of 80 mm by 80 mm by 12 mm was fabricated for preparing Mode III tear test specimens. Each side of the box represents a single extrudate wide wall, formed by multiple extrudates stacking up one over another: within each layer, there is only one continuous extrudate deposited as a hollow square. The width of the wall equals to the width of a single extrudate, which is set to be same with the nozzle diameter of 0.5 mm.

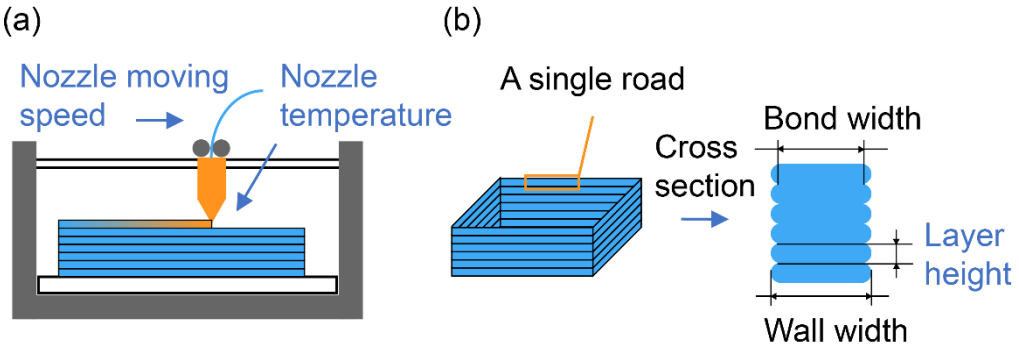

Fig. 1. Schematics of (a) fused filament fabrication process and (b) printed geometry of one-layer wide hollow box.

Three different processing parameters were separately varied during printing: layer height (0.05 mm to 0.45 mm), nozzle temperature (230 °C to 290 °C), and print speed (5 mm/s to 30 mm/s). All other parameters, including 115 °C build plate temperature, were set to be constant during this study, as noted in the section **S2** of Supplementary Materials.

2.3. Geometrical characterizations

As **Fig. 2(a)** shows, a 10 mm by 10 mm piece of single filament wall was cut and scanned by Bruker Skyscan 1172 Micro-CT scanner. With a resolution of 4.87 μm/pixel, the relevant geometric information, including wall width and bond width, could be measured and extracted by image analysis with MATLAB. The scanned geometry was further compared with the original design and other specimens with different processing conditions to gain a better understanding of how processing parameters influence printing geometry. Finally, to verify the accuracy of micro-CT measurement results, additional optical microscope measurements were conducted (see section **S3** of Supplementary Materials).

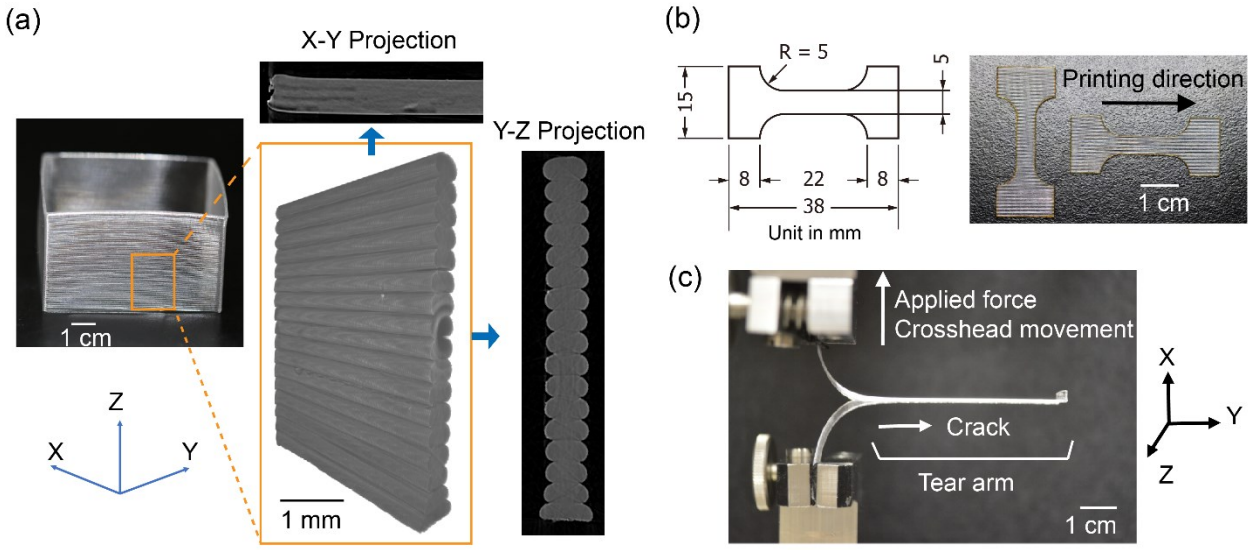

Fig. 2. (a) Reconstructed 3D geometry from micro-CT scans and its projections to two planes. (b) Geometry and pictures of laser-cut dogbone tensile specimens. (c) Tear test specimen and setup.

2.4 Mechanical characterizations

2.4.1 Uniaxial tensile test

Uniaxial tensile tests were performed with an Instron ElectroPlus E1000 tester based on the ASTM D1708 standard. As **Fig. 2(b)** shows, dogbone tensile specimens with 12 mm by 5 mm gauge area were fabricated with a VLS 6.60 laser cutter. Since heat from laser cutting can bring significant thermochemical effects like surface browning, painter's tape was attached on both sides of the single filament wall to shield the specimens and mitigate those effects. Through observation, the browning was greatly reduced (while not fully eliminated). For the cut edges, the polymer was molten and smoothed by laser cutting, which would minimize stress concentrations (see section **S4** of Supplementary Materials). For each set of processing parameters, at least 10 tensile specimens were fabricated and tested, with 5 specimens tested along printing direction (longitudinal test) and 5 specimens tested perpendicular to printing direction (transverse test).

According to the standard, the speed of testing is set to be 0.01 mm/s for quasi-static condition and yield point was reached around 100 s. During the tests, the strain around the gauge area was captured from videos taken on a Canon EOS 80D digital single-lens reflex (DSLR) camera (see section **S5** of Supplementary Materials). After the tests, nominal Young's modulus, nominal tensile strength and bonding strength were calculated based on force-displacement curves and specimen geometry. To be noted here, two different calculation approaches were used regarding different application scenarios. For engineering applications that do not account for the specimen's internal geometries, the tensile specimen is considered as a flat plate. Here the nominal tensile strength is calculated as the fracture force divided by the measured average initial cross-sectional area. Similarly, for the nominal Young's modulus, the stress was

calculated as force divided by measured average initial cross-section area, while the strain was analyzed from the pictures taken during tests. On the other hand, if we want to characterize the bonding quality, we need to look into the detailed structures. As the tensile specimen will fracture along the weakest bonding region (see section **S6** of Supplementary Materials), the measured bond width was used to calculate the bonding strength, which equals to fracture force divided by measured bonding area of 5 mm by bond width (< 0.5 mm, depending on printing parameters).

2.4.2 Tear test

Mode III tear tests were performed on the PC specimens. One-layer wide hollow boxes were printed and laser cut into specimens with area of 12 mm by 80 mm. In each of the specimens a crack was initiated at one end with a sharp razor such that the crack moves along the same direction as the printing direction. Then, this crack was propogated slightly before testing to prevent catastrophic failure and ensure a natural, sharp crack tip. For each set of processing conditions, 3 hollow boxes were printed resulting in 12 samples per parameter. Unlike the study presented in [14], the crack was initiated after the printing process, resulting a more uniform thermal history throughout the part. In addition, the parameter varied was the layer height; the print speed was set to 10 mm/s and the printing temperature was set to 280 °C.

The samples were oriented in the MTS Criterion 40 load frame as shown in **Fig. 2(c)**. The orientation is such that the direction out of the plane of the page is the Z-direction in the printing orientation. The positive X direction is the direction of printing. The face of the sample with a normal in the positive Y direction is on the inside of the hollow box. The samples were loaded with the MTS grips such that the tear arm was perpendicular to the loading direction. The crosshead displacement was fixed to 1 mm/s and data points (force and displacement) were taken at a frequency of 10 Hz. Videos were captured using a Canon EOS 3400 DSLR camera with a 16 mm extender lens. From the video, the radius of curvature of the sample behind the crack tip was calculated using the CircleFitByPratt algorithm written in MATLAB [39]. Due to rotation of the tear arm as the test progressed, the mode of the test deviated from the pure mode III to a mixed mode loading near the end of the tear test. To obtain a tear force for a sample, the force was averaged starting from the peak force point to the point that the displacement was equal to the radius of curvature. This average steady state force was converted to a tear energy using the Eq. (1) below. This equation was derived by assuming the work of crosshead displacement went directly into propagating the crack. Elastic strain energy and stored plastic energy were neglected.

$$E = 2 * \frac{F_{ss}}{w_b} \quad (1)$$

Where E is the tear energy in units of [N/mm], F_{ss} is the steady state force during tear test, w_b is the bond width.

2.5 Simulations

Simulations of the tensile tests were performed using commercial finite element package Abaqus/Standard. As shown in **Fig. 3**, a thin slice of scanned 3D geometry was converted into vector form and imported into Solidworks 2017 and exported to IGES, which could be read by Abaqus (see section **S7** of Supplementary Materials for details). The bottom surface was constrained in Z direction, while the bottom left corner point was fixed in all directions. A small displacement loading was applied on a reference point coupled with the top surface, while all other boundaries were set free to simulate the uniaxial tensile condition. The 8-node linear brick with reduced integration and hourglass control element (C3D8R) was used in simulations. The mesh size was determined by mesh convergence study, which found the optimum element size that balances between computational cost and prediction accuracy (see section **S7** of Supplementary Materials for details). Since we are investigating the elastic properties of tensile specimens, linear elastic material properties were applied in simulations, with Young's modulus of 1.82 GPa and Poisson's ratio of 0.35 (see section **S1** of Supplementary Materials for details). After the simulations, the reaction force on reference point was extracted, which equals the reaction force on the right loading surface. Then, based on the reaction force, loading displacement and geometry, the Young's modulus of tensile specimens was obtained and compared with experimental results.

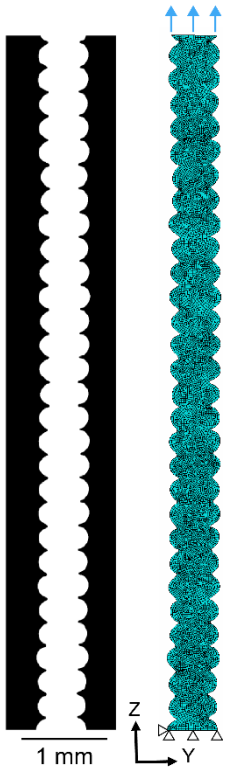

Fig. 3. Scanned cross section profile and converted finite element analysis setup.

3. Results and discussions

3.1 Effects of varying layer height

Samples with different layer heights ranging from 0.05 mm to 0.45 mm were prepared and scanned by micro-CT. From Y-Z cross sections of the reconstructed 3D model, we could obtain the pixel-to-pixel distribution of road widths along the stacking direction. As shown in **Fig. 4**, the maximum road width (the maximum value of the average road width within each layer) remained almost constant across different layer heights, while the average bond width decreases slightly with increase of layer height. For all scanned samples, the average widths were always larger than the designed wall width of 0.5 mm, indicating over-extrusion, which could be compensated by tuning flow parameters, as discussed in Section **3.4**. The biggest change happened on the bond width (minimum road width within two adjacent layers). The bond width decreased steadily as layer height increased. The reduction of bond width influences the mechanical behavior of printed products, reducing both Young's modulus and tensile strength.

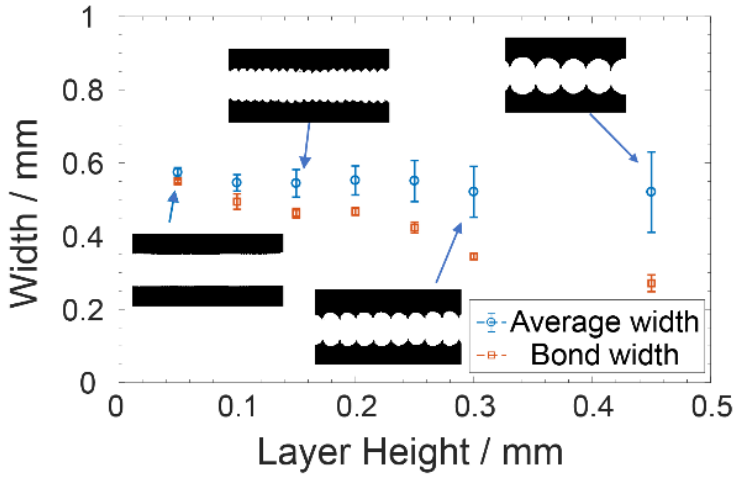

Fig. 4. Geometrical effects of changing layer height. The error bars are from standard deviations of data obtained from 5 measurements.

Uniaxial tensile tests were performed on samples with 0.15 mm, 0.30 mm, and 0.45 mm layer height. For longitudinal tests along printing direction, all stress-strain curves were calculated and plotted in **Fig. 5(a)**. All fifteen tested samples showed very similar stress-strain relationships, and the nominal ultimate tensile strengths (UTS) were 6% smaller than that of the bulk PC; while the Young's moduli were close to that of the bulk PC, as **Fig. 5(b)** shows.

For transverse tests perpendicular to printing direction, the stress-strain curves for three different layer heights tend to group by layer height as shown in **Fig. 5(c)**. For nominal UTS and Young's moduli, both values decreased with increasing layer height (**Fig. 5(d)**), which is consistent with the bond width decrease observed above. To correct for the decrease in bond width, the area measured from micro-CT was used to calculate an actual UTS and Young's modulus (**Fig. 5(e)**). Interestingly, we found there is only slight increase of the local bonding strength for different layer heights, and the absolute values are around 30 % smaller than bulk

PC's strength while the fracture strain was approximately 2.4 % for all samples, as plotted in **Fig. 5(f)**. This indicates the bonding area change is the main reason of strength reduction for different layer heights, and we could potentially predict the strength change by measuring the area of the bonding region.

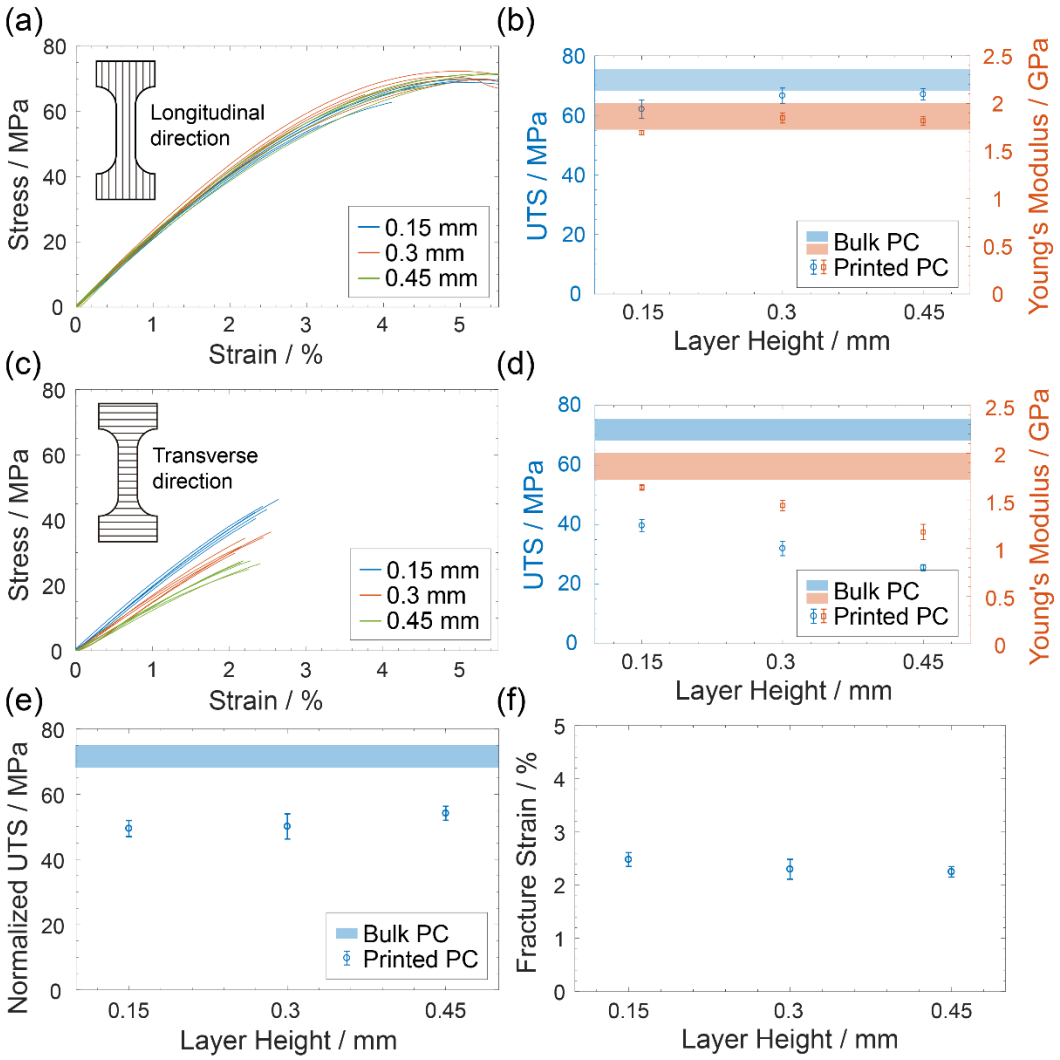

Fig. 5. Mechanical effects of changing layer height. (a) Stress-strain curves of longitudinal tests. (b) Ultimate tensile strength and Young's modulus results of longitudinal tests. (c) Stress-strain curves of transverse tests. (d) Ultimate tensile strength and Young's modulus results of transverse tests. (e) Transverse tests ultimate tensile strength normalized by scanned cross section area. (f) Fracture strain of transverse tests. The error bars are from standard deviations of data obtained from 5 measurements. The measurements of bulk PC properties are in section S1 of Supplementary Materials.

For nominal UTS, the fracture happens at the narrowest bond so that the bond width could be utilized to explain the mechanical change and calculate the material intrinsic bonding strength (**Fig. 5(e)**). For the reduction of modulus, the qualitative reason is same: the narrower bond decreases the entire specimen's stiffness. However, the quantitative explanation of modulus change is much harder, as both narrow and wide parts contribute to elastic deformation, neither

average width nor bond width completely capture the elastic response. As shown in **Fig. 4** and **Fig. 5(d)**, The change of Young's modulus is not a simple linear function of bond width: for the 0.15 mm layer height, the modulus is similar to that of bulk PC; for the 0.45 mm layer height, the reduction in modulus is 50% smaller than the reduction in bond width. As mentioned in the literature, multiple factors could influence the as-printed modulus, including geometrical dimensions and nozzle exit pressure [10,40]. To investigate the contribution of dimensional variation, here we performed finite element simulations. By using the measured geometry and a linear elastic material model, the simulated tensile behavior of FFF products were predicted and compared with measurements. As **Fig. 6** shows, the simulations give a good estimation of the modulus change within 5 % of deviation from measurements, which indicates geometry change contributes most to the modulus change.

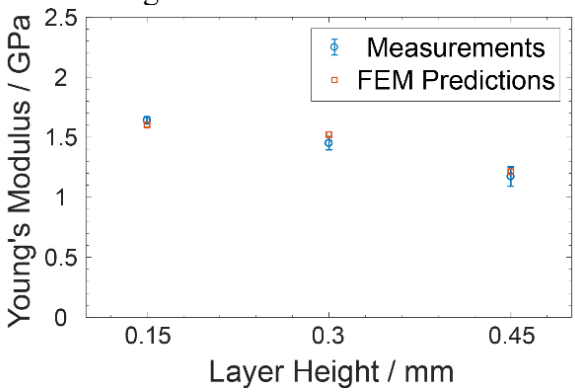

Fig. 6. Comparison between measured Young's modulus in transverse tests and the corresponding predictions from finite element method. The error bars are from standard deviations of data obtained from 5 measurements.

Next, we conducted Mode III tear tests to study the effects under shear loads as various loading conditions could be expected in engineering applications. Tear tests were performed on samples with layer heights of 0.15 mm, 0.3 mm, and 0.45 mm. The collated results are plotted in **Fig. 7**. The tear force was obtained using the method outlined in **Section 2.4.2**. These data show a steep decrease with increasing layer height; the 0.15 mm samples are much stronger than the other two layer heights. When plotting tear energy using the bond widths measured via micro CT by the procedure in **Section 2.3** the data shows that while the 0.15 mm layer height samples are still stronger than the others the difference between the 0.30 mm and the 0.45 mm has increased. Using ANOVA we can safely reject the null hypothesis with a p-value of 1.5 E-14 and conclude that the average tear energy values for each layer height are different. This indicates the cross-section geometry plays an important role in the tearing performance. The data show a strong relationship between the tear energy and the layer height, suggesting that decreasing the layer height increases the tear strength of the interface. Several factors may play a role in this development. Decreasing the layer height brings the hot nozzle closer to the previously deposited layer, which may increase the temperature of the interface and increase the isothermal welding time, leading to longer range chain diffusion and chain relaxation, making a better welding quality [41 - 44].

One caveat to this data, a noticeable amount of residual plasticity is seen in the tested samples, with the smaller layer heights showing the most residual curvature. Significant plasticity is expected due to the bending of the tear arms and is not accounted for as a method of energy dissipation in the Mode III tear test. The method outlined earlier to calculate tear energy assumes the energy from the crosshead motion is dissipated into elastic strain energy, which is assumed negligible, and the energy to propagate the crack. The differences in the width and shape between the different layer heights could contribute to differences in the stored plasticity in the tear test. Wider bond widths would have more plastic dissipation as there is more material to bend, implying the lower layer heights have an overvalued tear energy. Accounting for this stored plasticity in the tear arms to measure a change in the material properties of the weld would be the work of a future FE model.

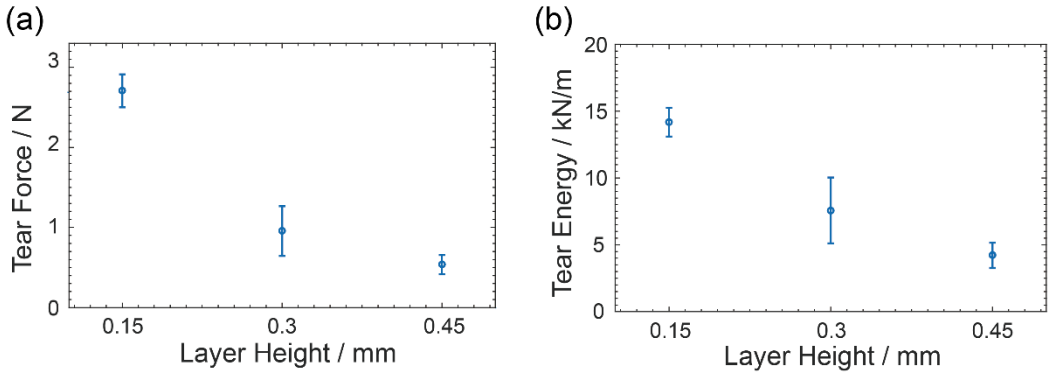

Fig. 7. (a)Tear force vs. layer height (b) Tear energy vs. layer height. The error bars are from standard deviations of data obtained from 12 measurements.

3.2 Effects of nozzle temperature

To study the effects of changing nozzle temperature, samples printed under 230 °C to 290 °C with 10 °C increment were scanned by micro-CT and analyzed. As **Fig. 8** shows, there was no significant change in the exterior geometry within this temperature range. Both the average and extreme values of road width remained similar.

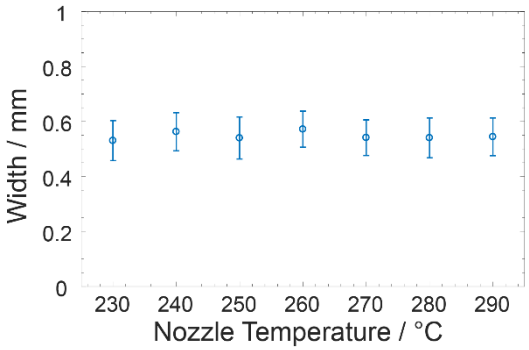

Fig. 8. Geometrical effects of changing nozzle temperature. The error bars are from standard deviation of data obtained from 5 measurements.

For each nozzle temperature, ten dogbone specimens were prepared and tested, with five of them stretching along the printing direction (longitudinal), and the others perpendicular to printing direction. For longitudinal tests, similar stress-strain curves were observed and no significant influence on nominal UTS and Young's modulus was found (**Figs. 9(a)-(b)**). The values of strength and modulus were close to those of bulk PC. However, nozzle temperature affected mechanical properties of samples loaded perpendicular to the print direction. As shown in **Figs. 9(c)-(d)**, the Young's moduli did not show clear trend with increasing nozzle temperature, while the nominal UTS increased with nozzle temperature at first, then reached a plateau after 250 °C. As shown in Fig. 8, no significant bond width change was observed for those samples, so that the strength loss below 250 °C should be due to other reasons, for example, the different thermal history. The welding quality between two adjacent layers heavily depends on the welding time, i.e., the duration that interlayer region remains hotter than glass transition temperature [41 - 44]. With higher nozzle temperature, the welding time will be longer, and the weld quality will be better. However, once enough interdiffusion and re-entanglement has occurred across the interface and reached equilibrium, longer welding times will not further increase the strength. Previous literature [9, 38] have shown the increasing trend of mechanical strength with higher fabrication temperature, while the plateau is observed in ABS but not PLA. This could be due to the relative difference between nozzle temperature, environmental temperature and glass transition temperature of the three polymers, as PLA has lower processing temperature (~200 °C) than ABS (~240 °C) and PC (~280 °C). Additionally, the different molecular weight may also contribute to this phenomenon.

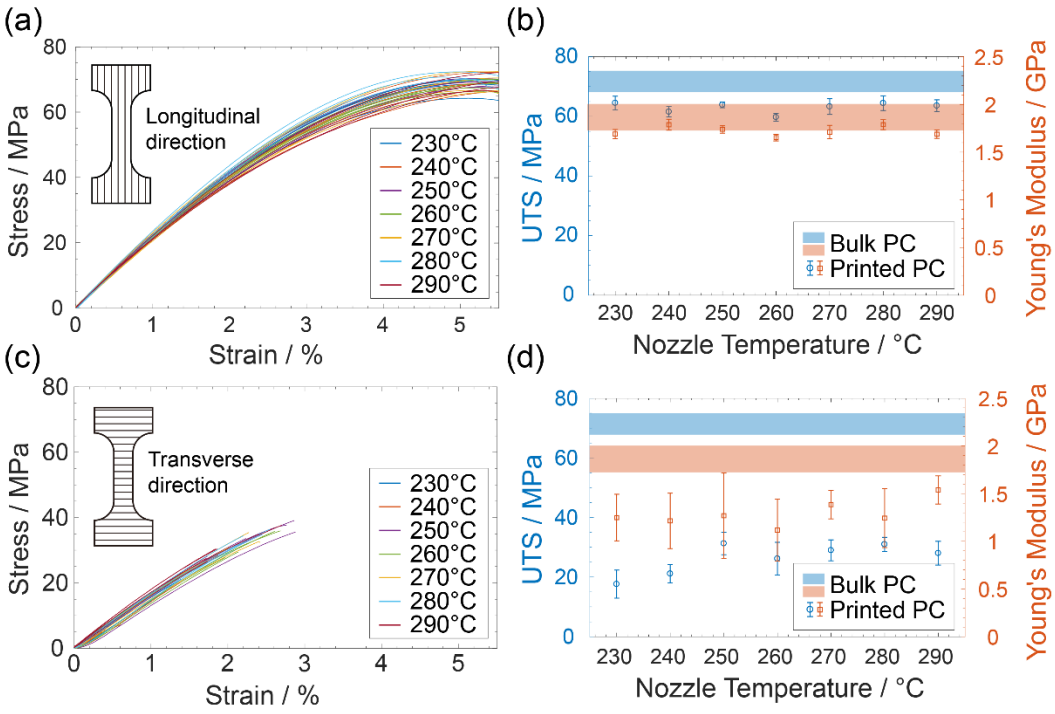

Fig. 9. Effects of the nozzle temperature on mechanical properties. (a) Stress-strain curves of longitudinal tests. (b) Ultimate tensile strength and Young's modulus results of longitudinal tests. (c) Stress-strain curves of transverse tests.

(d) Ultimate tensile strength and Young's modulus results of transverse tests. The error bars are from standard deviations of data obtained from 5 measurements.

3.3 Effects of varying print speed

To study the effects varying print speed, specimens with print speed ranging from 10 mm/s to 30 mm/s were fabricated and their geometrical and mechanical properties were characterized. As shown in **Fig. 10(a)**, geometrical defects could be visually observed for high print speeds. Visible defects appeared on the surface of 20 mm/s print speed sample and there was significant waviness when print speed reached 30 mm/s sample. From micro-CT scan, the defects on the 30 mm/s samples could be quantified as periodical change of road width along the printing direction: the wavelength was around 4 mm and the amplitude was around 0.2 mm. The potential causes of this defect are insufficient bonding between the first layer and the build plate, as well as flow instability. When printing at high print speed, the mismatch between nozzle moving speed and nozzle extrusion speed causes the very first layer to be dragged, experiencing high shear rate between the fast-moving upper part and the static bottom part, which can further cause insufficient bond with the build plate and then the meandering shape of the deposited extrudates.

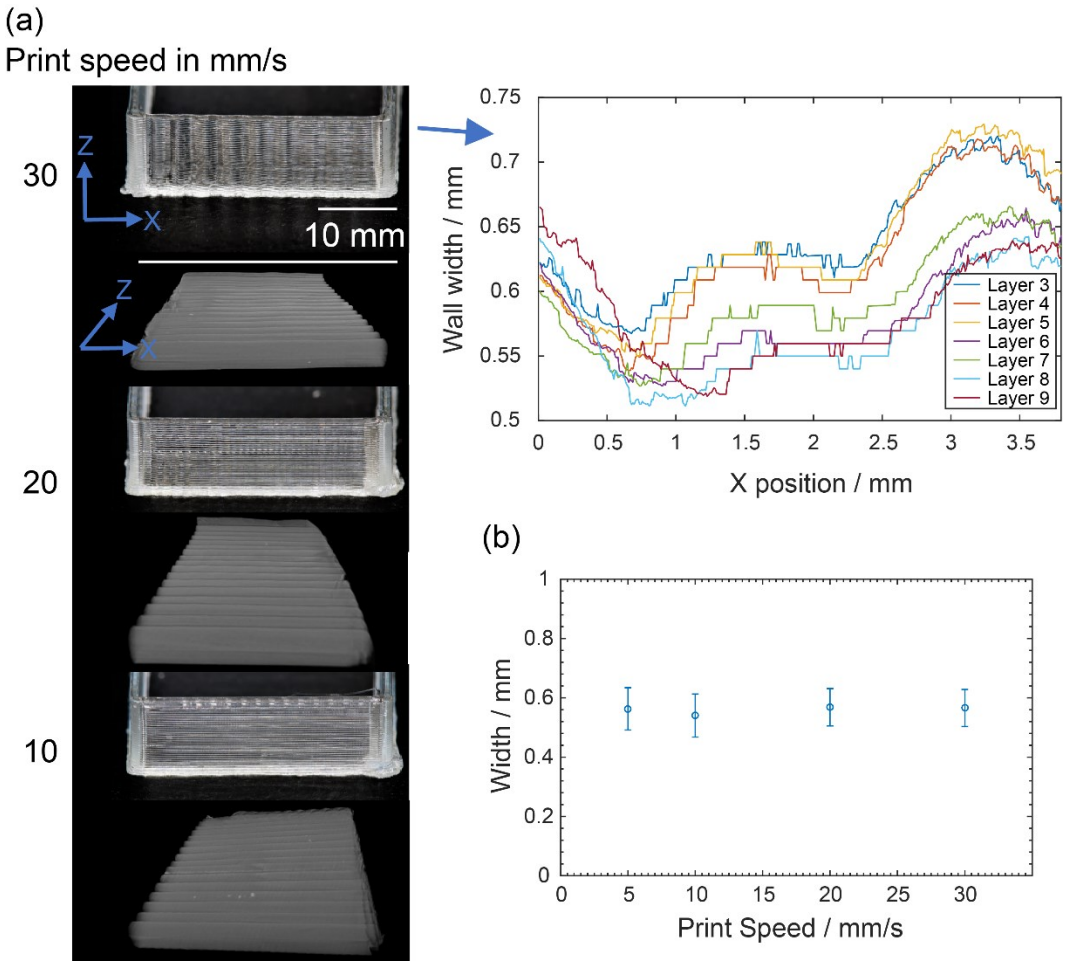

Fig. 10. (a) Geometrical effects of changing print speed. (Left) Defects start to appear at higher print speed. (Right) The micro-CT analysis of wavy patterns appeared for the 30 mm/s print. (b) Width of the specimens with changing print speed. The error bars are from standard deviations of data obtained from 5 measurements.

Interestingly, no significant mechanical performance change was observed for samples with different print speeds even with severe geometrical defects. As **Figs. 11(a)-(d)** show, for both longitudinal and transverse tests, the nominal UTS and Young's moduli remained similar across multiple print speeds ranging from 10 mm/s to 30 mm/s. These results could be due to the similar bond width and bonding quality within the tested range despite the waviness defects, as shown in **Fig. 10(b)**. Also, the trends are consistent with previous works [17], which suggests the mechanical performance remains similar before reaching a very high printing speed (~100 mm/s).

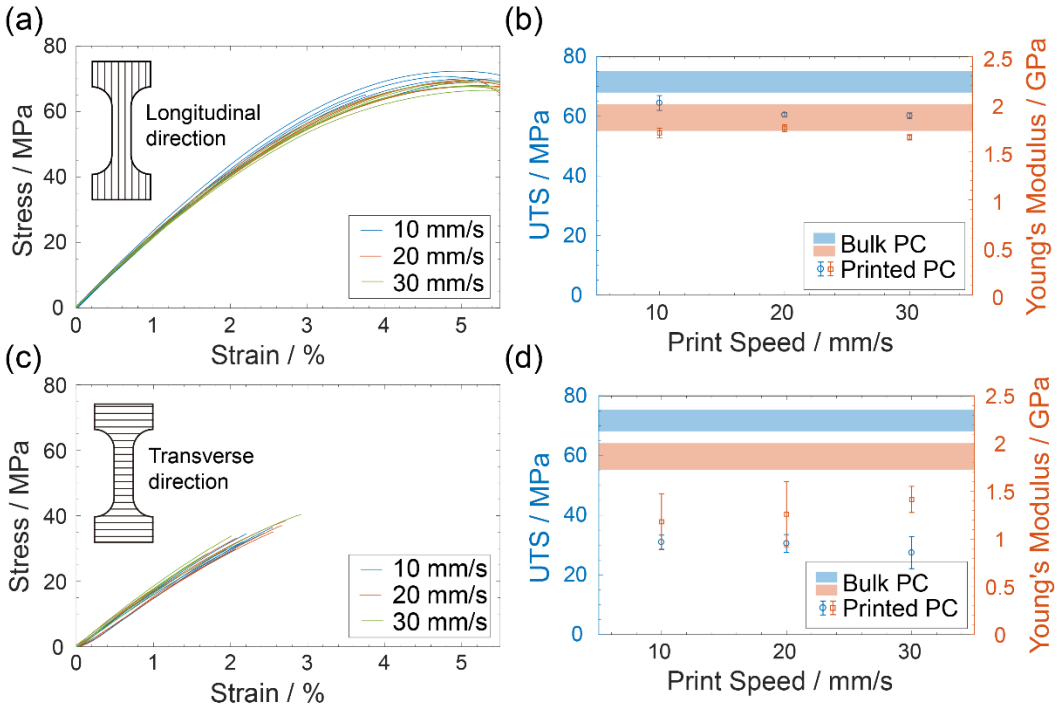

Fig. 11. Mechanical effects of changing print speed. (a) Stress-strain curves of longitudinal tests. (b) Ultimate tensile strength and Young's modulus results of longitudinal tests. (c) Stress-strain curves of transverse tests. (d) Ultimate tensile strength and Young's modulus results of transverse tests. The error bars are from standard deviations of data obtained from 5 measurements.

3.4 Compensation of over-extrusion

As mentioned in **section 3.1**, over-extrusions have been found in all printed samples. It could be a fabrication defect that varies from machine to machine. Due to die-swell effects, the volume control of extruded polymer is very sensitive to the normal stress, which is in turn sensitive to the capillary contraction, feed rate, and temperature. Hence small geometry or control errors in mechanical assembly or/and stepper motors could result in significant over-

extrusions. To compensate for those errors, we tuned the printing parameters as follows. For example, for the target width of 0.5 mm, the average road width measured by micro-CT was 0.523 mm. Since there is 4.6 % over-extrusion compared with the target dimension, we tuned the flow index to 95.6 % to limit the material feed and compensate the over-extrusion. After adjusting the flow index, we found the average road width changed to 0.504 mm, which gives much better geometrical accuracy (see section **S8** of Supplementary Materials for details). By using this method, micro-CT measurements could contribute to optimization of printing parameter selections for higher printing precision.

3.5 Discussion of Results

In **section 3.1**, the increase of both tensile and tear strength with decreasing layer height has been quantified and analyzed. From mechanical tests, the bonding strength is measured to be around 30% less than PC's intrinsic property, which makes the transverse direction always weaker than longitudinal direction. Then, combining with the micro-CT scan results, it is found that the geometry change at bonding regions further differentiates the strength of specimens printed with different layer heights. With higher layer height, the scalloping shape gives more variations in the width, and the narrower bonding regions, which are considered to be the weakest part, will deform and fracture earlier and reduce the whole specimen's strength. Based on the findings, decreases in layer height could be an easy way to improve mechanical performance, while users will suffer from extended printing time. Depending on different applications, a balance between strength and speed can be optimized. Meanwhile, the variation in Young's modulus opens a possible method for controlling the modulus of printed product by varying printing parameter like layer height, as we have shown the capability of predicting Young's modulus change by finite element analysis. For the next step, incorporating comprehensive finite element analysis to the tear behavior would help to gain more understanding on how printed products fail so that we can control the failure behavior by varying printing parameters.

In **section 3.2**, the effects of varying nozzle temperature were measured. For the PC filaments used in this study, the optimal nozzle temperature is above 250 °C, which is similar to the recommended value from the manufacturer. Lower nozzle temperatures reduce the bonding quality and decrease mechanical strength. In practice, users may find the material is still printable using printers that cannot reach designated nozzle temperature, but the mechanical performance could be compromised.

In **section 3.3**, it is shown that high print speed may lead to periodic geometry variation in printed products, while it did not harm the mechanical performance within the tested range. This finding suggests that if there is less requirement on geometric accuracy, increasing print speed could be a good method to improve printing efficiency while maintaining satisfactory mechanical performance, as the bonding area remains similar. However, if a smooth and flat exterior surface is desired, print speed should be limited to get good geometrical accuracy. Considering the main cause of waviness defect is poor bonding quality of the first layer, a

potential solution could be tuning printing parameters of the first layer separately, which is an available function in multiple pre-printing slicer software.

From our perspective, the mechanical performances of FFF specimens are directly controlled by the printed structures as well as the physical and chemical changes that occur during processing. However, the structural and property changes may not be sensitive to some processing parameters, which results in the insensitivity to those parameters. For varying print speed, the waviness defect shown in **Fig. 10(a)** does not influence the bonding area between two adjacent layers so that there is minimal effect on mechanical properties. For varying nozzle temperature, while the macroscopic geometry remains similar, the microscopic polymer chain formation changes significantly, causing the strength decrease at lower nozzle temperatures. Finally, for the layer height, this parameter strongly impacts the as-printed geometries, changing both bonding area and the uniformity along the stacking direction (z direction). Thus, it produces the greatest mechanical property changes among the three processing parameters studied.

From these findings, several suggestions for printing parameter selections can be proposed. First, the experiments further prove that a sufficient nozzle temperature should be used to give long enough welding time for a fully developed interlayer bond to have good geometrical and mechanical properties. For the Ultimaker PC used in this study, the recommended minimum nozzle temperature is 250 °C. Next, machine-related extrusion error may cause under- or over-extrusion of printing materials, and this can be compensated by measuring the extruded volume and tuning the flow index. For our LulzBot TAZ 6 printer and LulzBot Hexagon hot end tool head, reducing the flow rate by 4.4% provided better accuracy, resulting 0.8% error in geometric dimensions. Last, but most importantly, varying layer height and print speed will have a tradeoff of printing time, geometrical accuracy and mechanical performance. Users need to balance between them based on the constraints such as available print time, mechanical strength, and geometric variability.

4. Summary and Conclusions

In this work, we conducted both geometrical and mechanical characterizations of FFF-printed parts with varied processing parameters, then analyzed these results to understand the processing-structure-property relationships. When increasing layer height, the bonding area reduced, and it caused reductions in transverse tensile strength and Young's modulus. The strength and modulus change were correlated with geometry changes quantified with micro-CT scan results: the strength has simple linear relationship with the bonding area, while the modulus change is more complex but still could be explained by finite element simulations. For varying the nozzle temperature, no significant geometrical difference was found, but a minimum threshold of 250 °C was observed to reach maximum mechanical properties. If increasing print speed, there could be periodical geometry error in printed width, while it did not influence mechanical performance within the range that we tested.

This work serves as the first step of fully understanding the FFF process from interlayer bonding perspective. For the next step, it is necessary to extend the focus from a single filament

wall to complex 3D structures, where tool path and raster angle play important roles and intralayer bonding should to be considered and studied. In addition, advanced mechanical characterization tools, including Mode I peel tests and Mode III tear tests can be applied to all interested processing parameters. And finally, a multi-scale multi-physics computational model should be incorporated for full modeling of FFF process and predicting resulting properties.

Acknowledgements

We would like to acknowledge the support of the National Science Foundation (DMREF-1628974), and the start-up fund from the Whiting School of Engineering at Johns Hopkins University. We would like to thank Prof. Stavros Gaitanaros and Ms. Sirui Bi for allowing us to use their micro-CT machine and providing help. We also would like to thank Prof. Vicky Nguyen, Prof. Peter Olmsted, Prof. Mark O. Robbins, Mr. Zheliang Wang and Mr. Marco Galvani Cunha for helpful comments and suggestions regarding this study.

References

[1] I. Gibson, D.W. Rosen, B. Stucker Additive Manufacturing Technologies (2010)

[2]"ISO / ASTM52900-15, Standard Terminology for Additive Manufacturing - General Principles - Terminology." ASTM International.

[3] Lipson, Hod, and Melba Kurman. Fabricated: The new world of 3D printing. John Wiley & Sons, 2013.

[4] Ahn, Sung-Hoon, et al. "Anisotropic material properties of fused deposition modeling ABS." Rapid Prototyping Journal 8.4 (2002): 248-257. https://doi.org/10.1108/13552540210441166

[5] Anitha, R., S. Arunachalam, and P. Radhakrishnan. "Critical parameters influencing the quality of prototypes in fused deposition modelling." Journal of Materials Processing Technology 118.1-3 (2001): 385-388. https://doi.org/10.1016/S0924-0136(01)00980-3

[6] Chin Ang, Ker, et al. "Investigation of the mechanical properties and porosity relationships in fused deposition modelling-fabricated porous structures." Rapid Prototyping Journal 12.2 (2006): 100-105. https://doi.org/10.1108/13552540610652447

[7] Sun, Q., et al. "Effect of processing conditions on the bonding quality of FDM polymer filaments." Rapid Prototyping Journal 14.2 (2008): 72-80. https://doi.org/10.1108/13552540810862028

[8] Spoerk, Martin, et al. "Polypropylene Filled with Glass Spheres in Extrusion‐Based Additive Manufacturing: Effect of Filler Size and Printing Chamber Temperature." Macromolecular Materials and Engineering (2018): 1800179. https://doi.org/10.1002/mame.201800179

[9] Seppala, Jonathan E., et al. "Weld formation during material extrusion additive manufacturing." Soft Matter 13.38 (2017): 6761-6769. https://doi.org/10.1039/C7SM00950J

[10] Coogan, Timothy J., and David Owen Kazmer. "Bond and part strength in fused deposition modeling." Rapid Prototyping Journal 23.2 (2017): 414-422. https://doi.org/10.1108/RPJ-03-2016-0050

[11] Sood, Anoop Kumar, Raj K. Ohdar, and Siba S. Mahapatra. "Parametric appraisal of mechanical property of fused deposition modelling processed parts." Materials & Design 31.1 (2010): 287-295. https://doi.org/10.1016/j.matdes.2009.06.016

[12] Rayegani, Farzad, and Godfrey C. Onwubolu. "Fused deposition modelling (FDM) process parameter prediction and optimization using group method for data handling (GMDH) and differential evolution (DE)." The International Journal of Advanced Manufacturing Technology 73.1-4 (2014): 509-519. https://doi.org/10.1007/s00170-014-5835-2

[13] Riddick, Jaret C., et al. "Fractographic analysis of tensile failure of acrylonitrile-butadiene-styrene fabricated by fused deposition modeling." Additive Manufacturing 11 (2016): 49-59. https://doi.org/10.1016/j.addma.2016.03.007

[14] Ziemian, Constance, Mala Sharma, and Sophia Ziemian. "Anisotropic mechanical properties of ABS parts fabricated by fused deposition modelling." Mechanical Engineering. InTech, 2012.

[15] Sanatgar, Razieh Hashemi, Christine Campagne, and Vincent Nierstrasz. "Investigation of the adhesion properties of direct 3D printing of polymers and nanocomposites on textiles: Effect of FDM printing process parameters." Applied Surface Science 403 (2017): 551-563. https://doi.org/10.1016/j.apsusc.2017.01.112

[16] Kotlinski, Jaroslaw. "Mechanical properties of commercial rapid prototyping materials." Rapid Prototyping Journal 20.6 (2014): 499-510.

[17] Davis, Chelsea S., et al. "Mechanical strength of welding zones produced by polymer extrusion additive manufacturing." Additive Manufacturing 16 (2017): 162-166. https://doi.org/10.1108/RPJ-06-2012-0052

[18] Rodriguez, Jose F., James P. Thomas, and John E. Renaud. "Characterization of the mesostructure of fused-deposition acrylonitrile-butadiene-styrene materials." Rapid Prototyping Journal 6.3 (2000): 175-186. https://doi.org/10.1108/13552540010337056

[19] Boschetto, Alberto, and Luana Bottini. "Design for manufacturing of surfaces to improve accuracy in Fused Deposition Modeling." Robotics and Computer-Integrated Manufacturing 37 (2016): 103-114. https://doi.org/10.1016/j.rcim.2015.07.005

[20] Boschetto, Alberto, and Luana Bottini. "Accuracy prediction in fused deposition modeling." The international Journal of Advanced Manufacturing Technology 73.5-8 (2014): 913-928. https://doi.org/10.1007/s00170-014-5886-4

[21] Turner, Brian N., and Scott A. Gold. "A review of melt extrusion additive manufacturing processes: II. Materials, dimensional accuracy, and surface roughness." Rapid Prototyping Journal 21.3 (2015): 250-261. https://doi.org/10.1108/RPJ-02-2013-0017

[22] Kruth, Jean Pierre, et al. "Computed tomography for dimensional metrology." CIRP Annals-Manufacturing Technology 60.2 (2011): 821-842. https://doi.org/10.1016/j.cirp.2011.05.006

[23] Ashley, Steven. "Rapid prototyping for artificial body parts." Mechanical Engineering 115.5 (1993): 50.

[24] Berry, E., et al. "Preliminary experience with medical applications of rapid prototyping by selective laser sintering." Medical Engineering and Physics 19.1 (1997): 90-96. https://doi.org/10.1016/S1350-4533(96)00039-2

[25] Taud, Hind, et al. "Porosity estimation method by X-ray computed tomography." Journal of Petroleum Science and Engineering 47.3-4 (2005): 209-217. https://doi.org/10.1016/j.petrol.2005.03.009

[26] Rouholamin, Davood, and Neil Hopkinson. "Understanding the efficacy of micro-CT to analyse high speed sintering parts." Rapid Prototyping Journal 22.1 (2016): 152-161. http://dx.doi.org/10.1108/RPJ-03-2014-0030

[27] Kerckhofs, Greet, et al. "The combined use of micro-CT imaging, in-situ loading and non-rigid image registration for 3D experimental local strain mapping on porous bone tissue engineering scaffolds under compressive loading." Proceedings of European Conference for non-Destructive Testing (ECNDT). 2010.

[28] Du Plessis, Anton, et al. "X-ray microcomputed tomography in additive manufacturing: a review of the current technology and applications." 3D Printing and Additive Manufacturing 5.3 (2018): 227-247. https://doi.org/10.1089/3dp.2018.0060

[29] Nouri, Hedi, Sofiane Guessasma, and Sofiane Belhabib. "Structural imperfections in additive manufacturing perceived from the X-ray micro-tomography perspective." Journal of Materials Processing Technology 234 (2016): 113-124. http://dx.doi.org/10.1016/j.jmatprotec.2016.03.019

[30] Tronvoll, Sigmund A., et al. "A new method for assessing anisotropy in fused deposition modeled parts using computed tomography data." The International Journal of Advanced Manufacturing Technology (2019): 1-19. https://doi.org/10.1007/s00170-019-04081-7

[31] Chen, Roland K., et al. "Nano-CT characterization of structural voids and air bubbles in fused deposition modeling for additive manufacturing." ASME 2015 International Manufacturing Science and Engineering Conference. American Society of Mechanical Engineers, 2015. https://doi.org/10.1115/MSEC2015-9462

[32] Villarraga, Herminso, et al. "Assessing additive manufacturing processes with X-ray CT metrology." ASPE 2015 Spring Topical Meeting: Achieving Precision Tolerances in Additive Manufacturing, Raleigh, NC. 2015.

[33] Soete, Jeroen, et al. "Defect detection in 3D printed carbon fibre composites using X-ray Computed Tomography." https://www.ndt.net/article/ctc2019/papers/iCT2019_Full_paper_62. pdf (2019): 1-8.

[34] Guessasma, Sofiane, Sofiane Belhabib, and Hedi Nouri. "Significance of pore percolation to drive anisotropic effects of 3D printed polymers revealed with X-ray μ-tomography and finite element computation." Polymer 81 (2015): 29-36. https://doi.org/10.1016/j.polymer.2015.10.041

[35] Quan, Zhenzhen, et al. "Microstructural characterization of additively manufactured multi-directional preforms and composites via X-ray micro-computed tomography." Composites Science and Technology 131 (2016): 48-60. https://doi.org/10.1016/j.compscitech.2016.05.015

[36] Yu, Siwon, et al. "Analytical study on the 3D-printed structure and mechanical properties of basalt fiber-reinforced PLA composites using X-ray microscopy." Composites Science and Technology 175 (2019): 18-27. https://doi.org/10.1016/j.compscitech.2019.03.005

[37] Kerekes, Tomas Webbe, et al. "Characterization of process–deformation/damage property relationship of fused deposition modeling (FDM) 3D-printed specimens." Additive Manufacturing 25 (2019): 532-544. https://doi.org/10.1016/j.addma.2018.11.008

[38] Zekavat, Amir Reza, et al. "Investigating the effect of fabrication temperature on mechanical properties of fused deposition modeling parts using X-ray computed tomography." The International Journal of Advanced Manufacturing Technology 100.1-4 (2019): 287-296. https://doi.org/10.1007/s00170-018-2664-8

[39] Pratt, Vaughan. "Direct least-squares fitting of algebraic surfaces." ACM SIGGRAPH computer graphics. Vol. 21. No. 4. ACM, 1987. https://doi.org/10.1145/37402.37420

[40] Coogan, Timothy J., and David O. Kazmer. "Modeling of interlayer contact and contact pressure during fused filament fabrication." Journal of Rheology 63.4 (2019): 655-672. https://doi.org/10.1122/1.5093033

[41] Jud, K., H. H. Kausch, and J. G. Williams. "Fracture mechanics studies of crack healing and welding of polymers." Journal of Materials Science 16.1 (1981): 204-210.

[42] Kline, D. B., and R. P. Wool. "Polymer welding relations investigated by a lap shear joint method." Polymer Engineering & Science 28.1 (1988): 52-57.

[43] Wool, Richard P. Polymer interfaces: structure and strength. Hanser, 1995.

[44] Hart, Kevin R., et al. "Increased fracture toughness of additively manufactured amorphous thermoplastics via thermal annealing." Polymer 144 (2018): 192-204.

Supplementary Materials

Table of Contents

S1. Measurements of PC printing filaments

Measurements of tensile strength and Young's modulus of as-received filaments were performed using uniaxial tensile tests. Tests were performed on round specimens of the Ultimaker filament (2.85 mm diameter). The Ultimaker filament was annealed at 140 °C for approximately 1 hour, to both straighten it and relax the curvature developed by being wound around a spool. The filament was then clamped with serrated wedge grips (the Advantage Wedge 10 with serrated wedges) for round specimens, and pulled at a quasi-static strain rate of 10^{-3} (1/s). The Young's modulus and the peak stress of a representative sample are shown in **Fig. S1** (a plot of engineering stress vs. engineering strain). The values are taken from the average of 10 samples each and the range reported is one standard deviation and are tabulated in **Table S1**. The printed filament was printed from the stress relieved Ultimaker filament from a 0.5 mm wide nozzle in a LulzBot TAZ Single Tool Head v2.1. The nozzle was heated to 280 °C and suspended 30 cm above the print bed. The filament was extruded at a rate of 3 mm^3/s into a chamber held at 22 °C in ambient conditions. This filament was cut into straight 30 mm length sections and held with Bionix Vise grips and EnviroBath Optional Grip 0.9. They were pulled with a quasi-static strain rate of 10^{-3} (1/s). Both tests were run on an MTS Criterion Series 40 at ambient laboratory conditions. Samples were allowed to age after heat treatments for 72 hours.

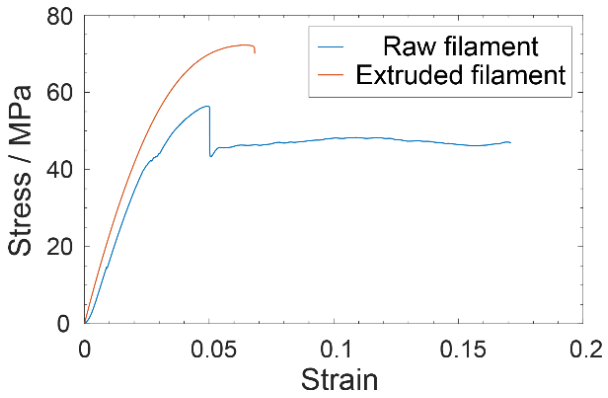

Fig. S1. Representative uniaxial tension plot of Ultimaker filaments before and after printing.

Table S1. Tabulated values of uniaxial tension specimens

	Diameter	Young's Modulus	Peak Stress
Bulk Filament	2.85 ± 0.02 mm	1.87 ± 0.13 GPa	71.6 ± 3.6 MPa
Printed Filament	0.46 ± 0.03 mm	1.82 ± 0.05 GPa	55.2 ± 6.1 MPa

S2. FFF process procedures and conditions

An open-source Lulzbot TAZ6 3D printer with 280 mm × 280 mm × 250 mm printing volume was used for sample fabrication. The print head we used is LulzBot hexagon hot end tool head with 0.5 mm nozzle diameter. This printer, equipped with all metal hot end, could heat up to 300 °C, and the build plate could heat up to 120 °C. For better heat uniformity across the build plate surface, we replaced the original one with Lulzbot TAZ modular print bed heater. To have

a low humidity environment for printing, a commercially available 3 mm-thickness acrylic enclosure (Printed Solid safety enclosure kit for Lulzbot TAZ 6) was added to the printer (**Fig. S2**). For convenient operation, we customized the front panel of the enclosure by making a 341 mm × 241 mm door through laser cutting.

To reduce printing defects, the polycarbonate filaments were dried in an oven (Lindberg/Blue M Vacuum Oven VO914C) at 100 °C for one hour before each printing process. During printing, in-house compressed air line was connected to the enclosure to continuously provide dry air into the system. Our experiments showed that the relative humidity (RH) inside the enclosure could be reduced to 10% RH within 10 minutes after turning on the compressed air. To monitor real-time environmental temperature and humidity during printing process, a USB multifunction datalogger (EXTECH Model RHT35) was added to this system. The data logs showed that all sample fabrication processes were conducted in room temperature and low humidity environment (⩽ 10% RH).

In sample preparation, the key processing parameters including layer height, print speed and nozzle temperature, were controlled and varied through the slicer Cura 3.2.32. All other parameters were set to be constant: the flow rate is set to be 100%, the nozzle diameter is 0.5 mm and the build plate temperature is 115 °C.

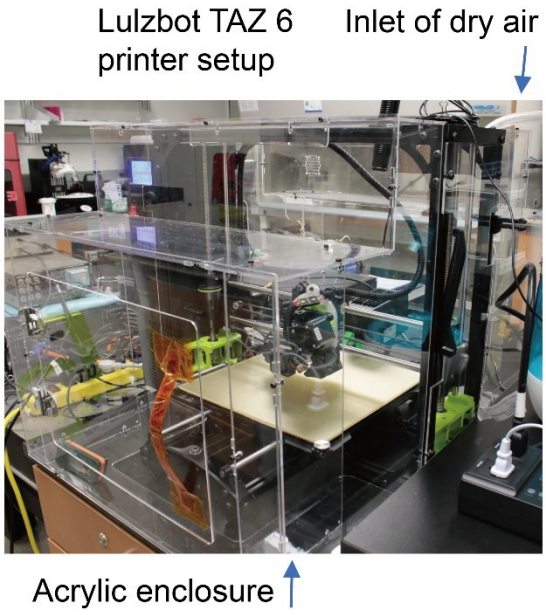

Fig. S2. Picture of the printer set-up used in this study.

S3. Validation of micro-CT measurements

To validate the micro-CT measurements based on post-processing, the cross-sections of the printed parts were characterized by an optical microscope. After micro-CT scans, a key parameter for post-processing is the threshold, which defines the signal level used in post-processing: if a region has higher-than-threshold readings, it is considered to be solid material;

otherwise it is considered to be air. As **Fig. S3(a)** shows, different threshold selections can lead to significant differences in reconstructed geometry. To validate our results, we used an IsoMet 1000 Diamond Blade Sectioning Saw to section our printed samples. The flat cross-section planes were then observed and captured with a Leica DM2700M optical microscope. The exact width was measured by counting pixels, which has a resolution of 1.07 μm per pixel, much better than 4.87 μm per pixel resolution of the micro-CT. The comparison between two results are plotted in **Fig. S3(b)**. Both results converged together within a range of threshold from 0.1 to 0.24. This indicates that we could get satisfactory micro-CT measurements using any of the threshold within the optimal range. While there are still little discrepancies between different layer and threshold, we chose 0.15 as the threshold in this study to get highest accuracy across all conditions.

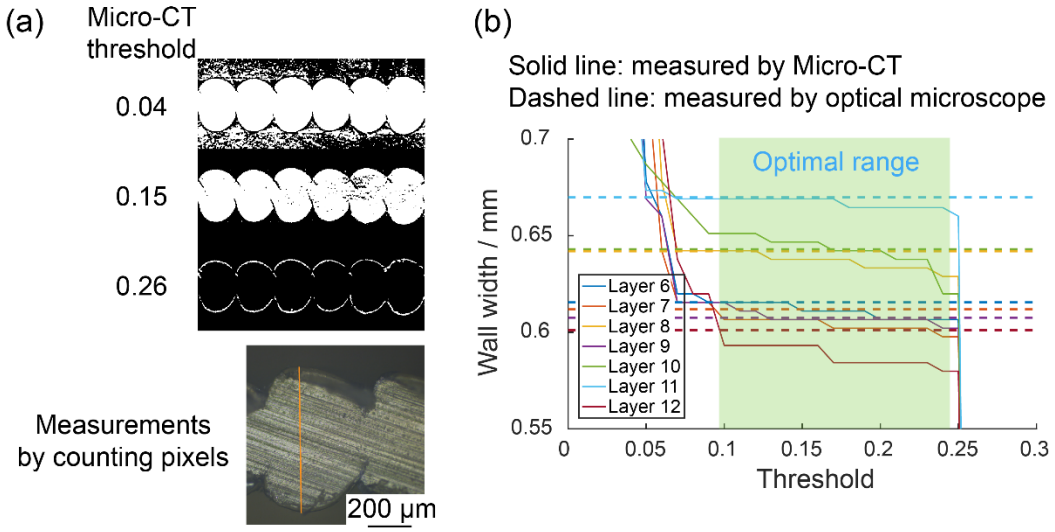

Fig. S3. Validation of micro-CT results. (a) The reconstructed geometry from micro-CT varies with post-processing threshold. To validate the results, the exact filament width was measured using optical microscope. (b) The CT results converge with the microscope-measured results within an optimal range of threshold.

S4. Laser cutting of printed specimens

As discussed in the main text, a protective paper tape was applied to mitigate surface browning brought by laser cutting. In **Fig. S4(a)** we show images of laser cut specimens with (top) and without (bottom) the tape, from which we could clearly see the specimen without tape has significant surface browning. Meanwhile, the laser also melted and smoothed the specimens' edges during processing, In **Fig. S4(b)**, the microscopic picture illustrates the smoothed edges so that edge effects were greatly reduced.

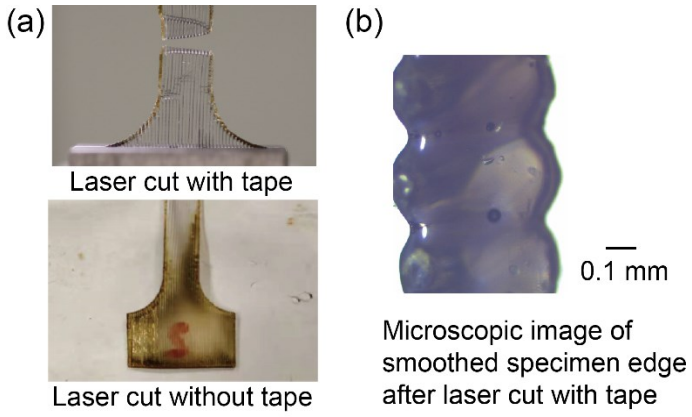

Fig. S4. (a) Comparison between different laser cut processes. (b) The microscopic side view of the cut showing the materials are molten and smoothed by laser cut with protective paper tape

S5. Measurement of strain

To measure the strain within gauge area during tensile tests, the stretching process was recorded, and ImageJ was used to post-process the images. **Fig. S5** shows the measurements we have done during this process. Firstly, before tests, the gauge length (in pixel numbers) and the distance between two grips were measured. Then, the image was captured at the time of interest and gauge length and grip distance were measured again. From those numbers, strain values in the gauge area were calculated as Eqs. (S1) and (S2):

$$\varepsilon_{gauge} = (L'_{gauge} - L_{gauge})/L_{gauge} \quad \text{(S1)}$$

$$\varepsilon_{grips} = (L'_{grips} - L_{grips})/L_{grips} \quad \text{(S2)}$$

As the movement of grips was recorded exactly by the tensile machine, L_{grips} and L'_{grips} are known, the gauge length could be calculated before and after deformation. To be noted here, as the surfaces of tensile specimens are not flat, DIC measurements did not work well in this study. Through some preliminary trials, the DIC generally had bad correlations, and it would give stochastic surface strain readings, which could not represent the real strain of test specimens.

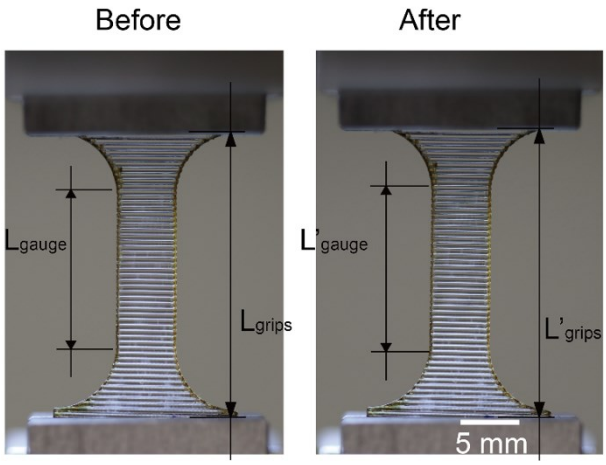

Fig. S5. Measurement of local strain.

S6. Sample fracture modes

Throughout the tensile tests, longitudinal tests (along printing direction) and transverse tests (perpendicular to printing directions) showed different failure modes. As shown in **Fig. S6**, longitudinal samples had ductile failure. The specimen firstly yielded, formed necking zone, then the crack initiated at one side and propagated until the entire sample reached a complete failure. Conversely, the transvers samples fractured brittlely. There was no sign before the specimen reached a sudden catastrophic failure. As observed, the cracks in transverse samples formed along the bonding interface, which is an expected result since the bonding zone has minimum area and strength.

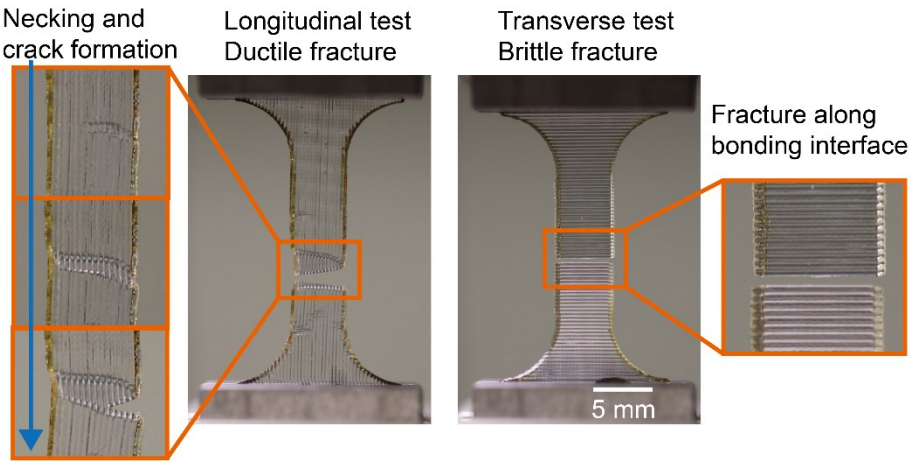

Fig. S6. Sample fracture modes.

S7. Finite element analysis

As shown in **Fig. 3** in main text, a cross section image was extracted from reconstructed 3D geometry and converted into a binary image. The outline of the specimen was further fitted and converted into vector form. The DXF (Drawing Exchange Format) file was then imported to Solidworks and transformed into Abaqus-readable IGES format, before finally modeled in the FEA using Abaqus. To validate simulation results, mesh convergence study was conducted. Different mesh sizes with the number of meshes ranging from 300 to 24,000 were used to estimate the error as **Fig. S7**. From the figure, the results converged to less than 0.2% error starting from 2,700 (= 0.27×10^4) meshes and the corresponding mesh density was used in simulations. This setup could be applied to all simulations as they share very similar overall dimensions.

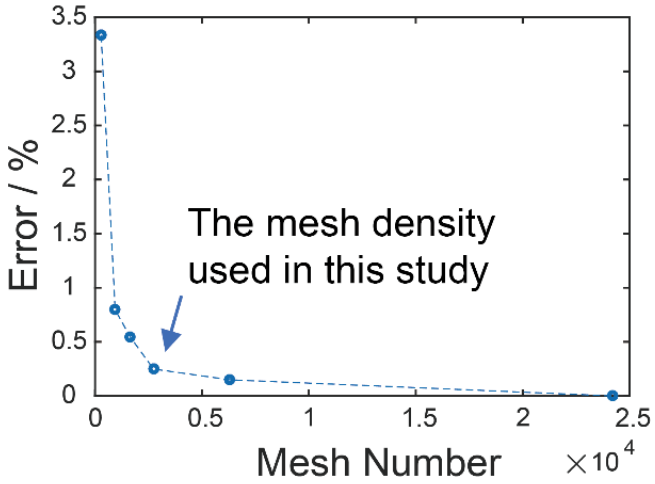

Fig. S7. The mesh convergence study.

S8. Compensation of over-extrusion

As shown in **Fig. S8**, the specimen printed with compensated flow index is slimmer than original settings. Through micro-CT scans and image processing, its average fiber width (0.504 mm) is much closer to the target width (0.5 mm), which indicates the over-extrusion defect is successfully mitigated.

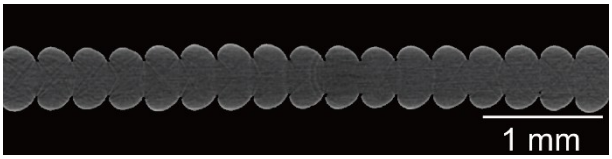

Fig. S8. Scanned cross section of specimen printed with optimized flow index.